

Implementation of an Integrated Homogeneous Heating and Fluorescence Detection Device for Microfluidic Point-of-Care (POC) Diagnosis of Tuberculosis

Jehad Alibaser, Erwin Realizan, Robby Zablan, Ralph Maru Grande, Rafael Pangilinan, Marc Rosales,
John Richard Hizon, Maria Theresa de Leon

Electrical and Electronics Engineering Institute,

University of the Philippines Diliman,

Quezon City, Philippines

jehad.alibaser@eee.upd.edu.ph, erwin.realizan@eee.upd.edu.ph, roddy.zablan@eee.upd.edu.ph,
ralph.grande@eee.upd.edu.ph, rafael.pangilinan@eee.upd.edu.ph, marc.rosales@eee.upd.edu.ph,
richard.hizon@eee.upd.edu.ph, theresa.de.leon@eee.upd.edu.ph

Abstract—This paper presents the development and validation of a compact microfluidic point-of-care (POC) device that integrates homogeneous heating with fluorescence-based detection in molecular assays for the diagnosis of tuberculosis. A copper thin-film microheater controlled by a PID algorithm enables rapid heating to 65°C within one minute and maintains thermal stability within $\pm 1^\circ\text{C}$ over an hour-long period. Thermal imaging and histogram analysis confirm temperature uniformity, with over 97.6% of readings falling within 64.5–65.5 °C, and the system demonstrates rapid recovery from external thermal disturbances. The fluorescence detection module, using AS7343 spectral sensors and blue LED excitation, was evaluated using LAMP mixes of two gene targets from *M. tb.*: *gyrA* and *atpE* mixes. Fluorescence readings effectively distinguished positive and negative samples, with clear thresholds emerging at approximately 10,000 units for *gyrA* and 6,000 units for *atpE*. The results strongly agree with assessments from the UPM National Training Center for Biosafety and Biosecurity (UPM-NTCBB), demonstrating the system's sensitivity and reliability. These outcomes support the device's suitability for accurate, low-cost molecular diagnostics in resource-limited or field-based settings.

Index Terms—Point-of-Care Testing, Microheater, PID, Fluorescence Detection, Embedded Systems.

I. INTRODUCTION

The demand for rapid and accessible diagnostic testing for tuberculosis has grown significantly in recent years. While polymerase chain reaction (PCR) remains the gold standard for accuracy, its high cost and slow turnaround time highlight the need for alternatives. Point-of-care testing (POCT), which allows diagnostic tests to be performed near the patient, emerged as a practical solution due to its speed, portability, and convenience [1].

Despite these advantages, many POCT systems still face challenges related to scalability, energy consumption, and accessibility in remote or low-resource settings [2]. One promising approach to address these issues is through microfluidic technologies. Often referred to as lab-on-a-chip systems, mi-

crofluidic devices combine multiple laboratory processes into a compact, integrated platform capable of handling small fluid volumes efficiently. Their size and simplicity allow for faster reaction times and improved portability, making them ideal for use outside traditional laboratory environments [3].

Recent innovations include paper-based microfluidic devices that work with portable readers and smartphones for applications such as tear fluid analysis [4]. These developments show the potential of microfluidics to streamline diagnostics and increase accessibility.

Temperature control is critical to many microfluidic processes, especially for nucleic acid amplification. Loop-mediated isothermal amplification (LAMP) is a promising alternative to PCR, as it operates at a constant temperature and eliminates the need for thermal cycling [5]. This makes LAMP more suitable for microfluidic integration, particularly when combined with low-power heating methods such as thin-film copper microheaters. Previous studies have demonstrated designs with reasonable power consumption, although achieving uniform heating remains a challenge [6].

Fluorescence detection is another essential function for microfluidic diagnostic systems. Sensors like the AS7262 have been shown to outperform older models such as the TCS3200 by offering multiple spectral channels in a compact package [7, 8]. The newer AS7343 sensor further improves on this by increasing the number of detectable wavelengths and reducing power consumption. It also features adjustable gain and integration time, which further enhances its accuracy and ability to detect signals in low-light conditions. However, there is still limited research on its performance in practical diagnostic setups.

This study aims to develop an integrated microfluidic platform that combines homogeneous heating using a copper microheater with fluorescence detection based on the AS7343 spectral sensor. The rest of this paper is organized as follows:

TABLE I: Material properties of the microheater.

Section II presents the specifications and architecture of the system, the Section III describes the materials, methods, and the results for the heating system, then followed by the fluorescence detection system in Section IV. Section V presents the whole system's architecture. Lastly, Section VI provides concluding remarks.

II. SYSTEM ARCHITECTURE AND SPECIFICATIONS

LAMP reactions typically require sustained homogeneous heating to successfully amplify a target nucleic acid. The LAMP protocol being used in UP Manila - National Training Center for Biosafety and Biosecurity (UPM-NTCBB) for TB detection requires a continuous heating at 65°C for 1 hour for amplification and a stop reaction at 80°C immediately after. To confirm successful amplification, SYBR Green is used as a fluorescent dye that binds to double-stranded DNA. Under blue light from an LED, it emits fluorescence, allowing for sensor-based detection suitable for portable diagnostics. The subsequent sections of this paper will discuss the methods and corresponding results obtained in meeting the required specifications.

III. HEATING SYSTEM

A. Microheater Design

The microheater design adopts a meandering pattern to achieve a homogeneous thermal distribution across the heating area. Each conductive strip has a track width of 2 mm, a spacing of 0.75 mm, and a copper thickness of 35 μm . The total length of the copper trace is approximately 880 mm, ensuring sufficient resistance for Joule heating [9]. The overall dimensions of the heater are 88 mm \times 33 mm, with an effective heating area of 70 mm \times 30 mm. These dimensions are designed to accommodate a 45 mm \times 17 mm LAMP heating region in a microfluidic chip while allowing compatibility with a broader range of microfluidic applications. Copper was selected as the heating material due to its high thermal and electrical conductivity and widespread use in PCB fabrication. The finalized geometry of the microheater is illustrated in Fig.. 1.



Fig. 1: Final geometry of the fabricated copper microheater with meandering pattern. Track width: 2 mm; copper thickness: 35 μm ; copper trace length: 880 mm; overall dimensions: 88 mm \times 33 mm.

B. Microheater Simulation

COMSOL Multiphysics was used to simulate the behavior of the microheater prior to fabrication. The materials used and their properties are shown in Table I. A 1 mm-thick aluminum layer was used as a heat spreader, covering the entire heating area to improve thermal distribution. The substrate used was FR-4, a common material in PCBs. Moreover, a PET film was placed between the copper microheater and the aluminum heat spreader.

Material	Density (Kg/m ³)	Electrical Conductivity (S/m)	Thermal Conductivity (W/m·K)	Heat Capacity (J/K·K)
Cu	8960	5.81×10^7	401	384
Al	2700	3.77×10^7	237	897
FR-4	1900	0.004	0.3	1369
PET	1350	0.004	0.2	1275

Two final configurations were evaluated: one incorporating a back copper heat spreader and another without it. COMSOL simulations showed that both designs exhibited uniform temperature profiles, with a maximum temperature difference of approximately 0.3 °C throughout the heating area. The designs were subjected to the same electrical conditions of 5 A and 0.987 V. Results indicated that the configuration without the back copper heat spreader achieved a higher overall temperature of around 85 °C, whereas the version with the heat spreader reached only 65 °C. Consequently, the back copper layer was excluded in the final design, shown Fig. 5, to improve thermal efficiency.

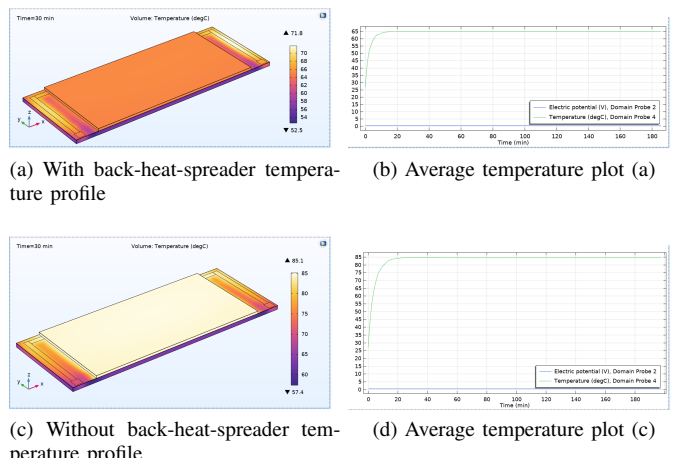


Fig. 2: COMSOL simulation results: (a) With back-heat-spreader temperature profile, (b) Temperature plot, (c) without back-heat-spreader, and (d) Temperature plot.

C. Heater Driver and Controller

1) *Thermistor:* The heating system was designed to maintain a controlled temperature environment suitable for DNA amplification. Temperature sensing was performed using an NTC thermistor, which was characterized through the Steinhart–Hart equation:

$$\frac{1}{T} = A + B \ln(R) + C(\ln(R))^3 \quad (1)$$

where T is the temperature in Kelvin, R is the thermistor resistance, and A , B , and C are empirically derived coefficients. The Steinhart–Hart equation was chosen because it provides an accurate mathematical model to relate the thermistor's resistance to temperature over a wide range, accounting for the nonlinear behavior of NTC thermistors. Resistance measurements at known temperatures were taken to calculate these coefficients and calibrate the thermistor for accurate real-time temperature measurement.

2) *Driver Circuit*: The heating element was driven by an IRLZ34N N-channel MOSFET acting as a low-side switch. The gate of the MOSFET was controlled by a PWM signal generated from a hardware timer of the STM32F411RE microcontroller, allowing precise modulation of power supplied to the heater. The gate voltage from the microcontroller is 3.3 V, which, according to the datasheet, is expected to produce approximately 6 A of current. It is higher than the 5 A required by the heater, as observed in the simulation. Moreover, to prolong the life of the MOSFET and reduce excess heating, the maximum PWM duty cycle was limited to 70% in the control code.

3) *PID Controller*: Temperature regulation was implemented using a PID (Proportional-Integral-Derivative) control algorithm programmed into the microcontroller. The control action is based on the error signal, defined as the difference between the desired temperature setpoint T_{set} and the measured temperature $T(t)$:

$$e(t) = T_{\text{set}} - T(t) \quad (2)$$

The PID controller calculates the control output $u(t)$ (which adjusts the PWM duty cycle) by combining three terms proportional to the error, the integral of the error, and the derivative of the error:

$$u(t) = K_p e(t) + K_i \int_0^t e(\tau) d\tau + K_d \frac{de(t)}{dt} \quad (3)$$

where the PID gains used in the system are:

$$K_p = 14.0, \quad K_i = 0.95, \quad K_d = 1.0 \quad (4)$$

All PID parameters were initially set to zero. Tuning was performed manually by first increasing K_p , followed by K_d , and finally K_i , in order to optimize system stability, minimize overshoot, and achieve a fast settling time in maintaining the temperature setpoint.

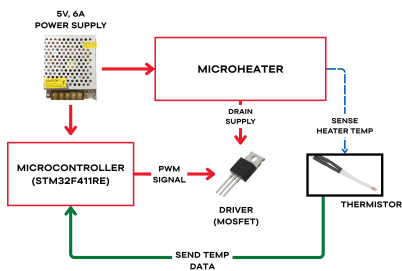


Fig. 3: Heating system flow diagram showing the signal flow for the PID control

Figure 3 illustrates the overall heating system flow diagram, highlighting the key components: the power supply, microcontroller, microheater, thermistor, and MOSFET. These elements work together to maintain a controlled temperature environment.

D. Fabricated Heater Homogeneity

The thermal images obtained using a FLIR TG267 Thermal Imaging Camera (see Fig. 4) demonstrate a relatively uniform temperature profile, indicating effective thermal homogeneity essential for reliable temperature control in sensitive applications.

Visible outlines in the images correspond to auxiliary materials, such as thermal tapes or markers, applied to enhance surface emissivity and improve the accuracy of temperature measurements by the infrared camera.

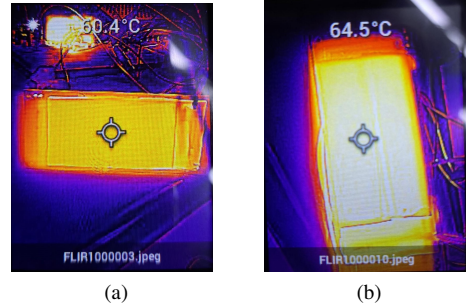


Fig. 4: Infrared thermal images of the fabricated microheater during operation.

E. Temperature Response

The performance of the heating system was evaluated based on its ability to rapidly reach and maintain the desired setpoint temperature suitable for DNA amplification. The system was subjected to a temperature profile test over a 60-minute period, with the temperature readings of the thermistor recorded at 2-second intervals. The results are summarized in Fig. 5.

1) *Initial Heating Phase (0-5 Minutes)*: In Fig. 5a the temperature response is shown during the initial 5 minutes. A rapid increase in temperature was observed, with the system reaching approximately 90% of the 65°C setpoint within the first 1 minute. A slight overshoot occurred just before stabilization, peaking in 66.51°C, which quickly settled back near the setpoint. This demonstrates a fast thermal response and minimal overshoot, which is an indicative of a well-tuned PID controller.

2) *Long-Term Stability (Full 1-Hour Profile)*: Fig. 5b presents the full 60-minute temperature profile. After reaching steady-state, the system maintained temperature stability within a narrow fluctuation band of $\pm 1^\circ\text{C}$ around the 65°C setpoint which was the tolerance set by UPM-NTCBB for reaction temperature. While occasional dips below 64.0°C were recorded, these were only present when the acrylic load was placed. This high level of regulation confirms the reliability of the PID algorithm in maintaining consistent conditions, which is critical for isothermal amplification reactions like LAMP.

3) *Temperature Distribution After Stabilization*: The histogram shown in Fig. 5c illustrates the frequency distribution of temperature values collected after the system stabilized. The data is tightly clustered around 64.5–65.5°C, with 97.6% of the total readings after the first 5 minutes falling within this range. Furthermore, temperature values ranging from 64 °C to 66 °C account for all data from 5 minutes to 1 hour. This

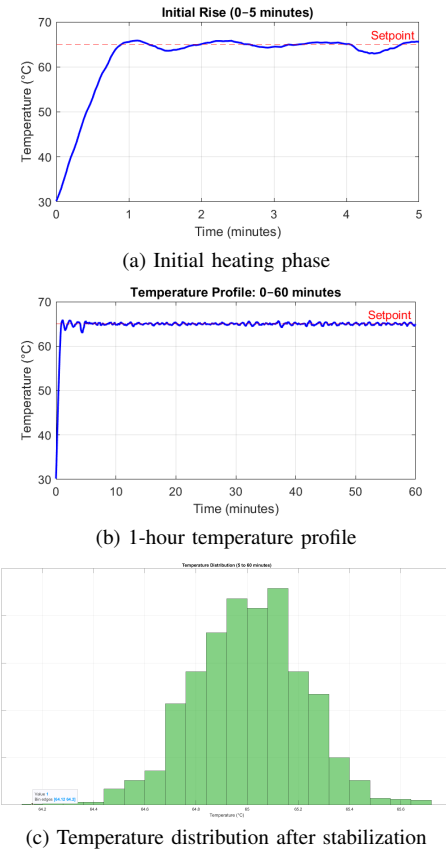


Fig. 5: Heating system performance

narrow distribution further confirms the uniformity and consistency of the heating system during steady-state operation.

Overall, the heating system successfully achieved fast ramp-up, minimal overshoot, and excellent long-term thermal stability, which are all key characteristics necessary for homogeneous heating in microfluidic point-of-care testing applications.

4) Load Impact on Temperature: The effect of placing a 4 mm acrylic load to the microheater is shown in Fig. 6 at approximately 4 minutes in the testing period, the temperature dropped from around 65 °C to a minimum of 62.96 °C. After this brief dip, the system began to heat up again, gradually returning to steady-state within 1 minute. This response demonstrates the heater's ability to recover from sudden thermal disturbances and maintain overall temperature stability critical for reliable operation.

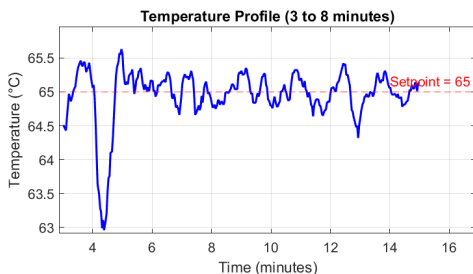


Fig. 6: Heating system response to a 4 mm acrylic load applied to the heater

5) Full Thermal Cycle Overview: Figure 7 provides a complete overview of the entire thermal sequence, starting

from the initial ramp-up to 65 °C, followed by sustained heating during the reaction phase. After maintaining a stable temperature of 65 °C for 1 hour, the system ramps up to 80 °C as a final processing step or deactivation phase. The temperature rises until it reaches 79.09 °C at approximately 1.3 minutes, holds this temperature for around 2 minutes, and then passively cools down. This comprehensive profile illustrates the heating system's capability to manage all required stages in the thermal workflow, including controlled shutdown.

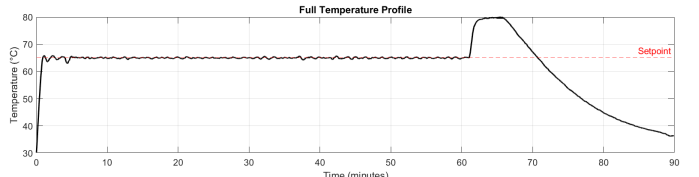


Fig. 7: Heating system performance for the whole duration from ramping up to setpoint, stop condition, and cooling down

F. Heater Power Consumption

The heater exhibits a peak power consumption of approximately 7.8 W during the initial ramp-up phase. Once steady-state conditions are reached, the power consumption stabilizes at approximately 1.2 W.

IV. FLUORESCENCE DETECTION SYSTEM

A. Flow Diagram and Setup

The fluorescence detection system uses six diffused blue LEDs (460–470 nm) to excite SYBR Green dye paired with AS7343 spectral sensors for detecting the emission, which fluoresces upon binding to double-stranded DNA. Each LED-sensor pair is aligned with a 0.2 mL microcentrifuge tube.

To minimize optical interference, physical dividers provide isolation between adjacent tubes, as shown in Fig. 8. The LEDs were positioned to avoid direct contact with the tubes, and sensor apertures were dimensioned for efficient signal capture.

The AS7343 sensor offers 14 spectral channels (380–1000 nm) with configurable gain and integration time for enhanced sensitivity. Since all sensors share the same I²C address, a TCA9548A multiplexer was used to enable individual communication, controlled by the microcontroller.

The system was tested using two types of sample mixes provided by UPM-NTCBB. Sensor readings were compared to their visual assessments and agarose gel electrophoresis results, allowing evaluation of detection reliability.

The overall system flow is illustrated in Fig. 9.

B. Fluorescence Detection Results and Analysis

The fluorescence detection system was evaluated using two sample sets of gene targets: *gyrA* and *atpE*. Measurements were recorded using AS7343 spectral sensors with a 256× gain and a 1000 ms integration time. These settings were chosen because they provide a balance between sensitivity and signal stability. Higher gain or longer integration times tended to cause signal saturation, while lower values reduced sensitivity. The selected settings ensured that positive samples produced noticeably higher signals than negative ones.

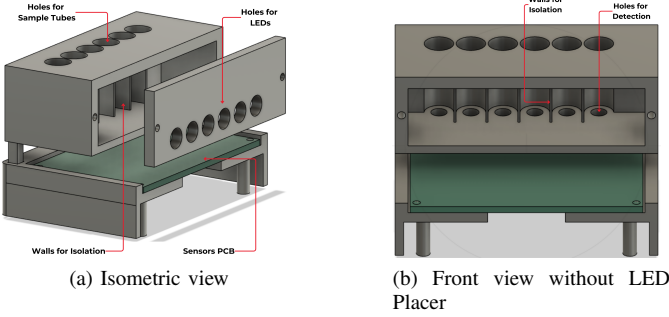


Fig. 8: 3D model of the fluorescence detection enclosure showing sensor alignment and optical isolation features.

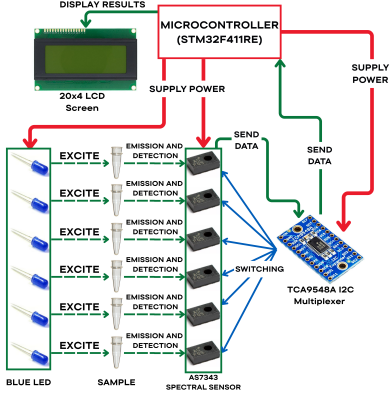


Fig. 9: Fluorescence detection system flow diagram

1) *gyrA Mix 1*: This set included an empty tube, three replicates of no template controls (NTC1, NTC2, NTC3), and samples with varying DNA copy numbers per microliter ranging from 10^0 to 10^5 with three replicates per sample. The empty tube showed the lowest fluorescence (2,850 units), serving as a baseline. Negative samples like NTC1 (6,050 units) and replicate 1 of 10^1 DNA copy numbers (5,739 units) had significantly lower readings than positive samples, which ranged from about 10,500 to 22,400 units, with the highest value at 22,404 (NTC3). Despite unexpectedly high readings in NTC2 and NTC3, a clear distinction exists between most negative and positive samples. A threshold of 8,324 units is proposed to classify samples as negative (below) or positive (above). These differences, illustrated in Figure 10, demonstrate the fluorescence system's ability to distinguish sample types in the *gyrA* mix 1 assay, consistent with UPM-NTCBB data.

2) *atpE Mix*: Fluorescence intensity data from the detection system were compared with reference results obtained using visual imaging and agarose gel electrophoresis of *atpE* gene target in *Mycobacterium Tuberculosis* from the UPM-NTCBB for the *atpE* mix samples. Sensor readings ranged from 2,850 units for the Empty slots to over 11,000 units for the highest samples. Positive samples (e.g. replicate 1 of 10^5 DNA copy numbers, and replicate 2 of 10^7 DNA copy numbers) generally showed fluorescence above 6,000 units, while negatives (e.g. replicate 1 of 10^4 DNA copy numbers, and replicate 1 of 10^1 DNA copy numbers) were mostly below 6,000 units. A threshold of 6,755 units effectively distinguishes positive

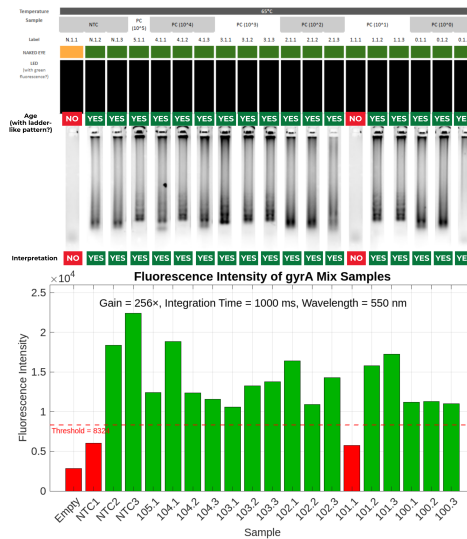


Fig. 10: Bar graph of fluorescence intensity measurements for *gyrA* Mix 1 samples together with the results from UPM-NTCBB.

from negative samples, aligning well with UPM-NTCBB classifications. These results, shown in Figure 11, confirm the fluorescence system's reliability for this assay.

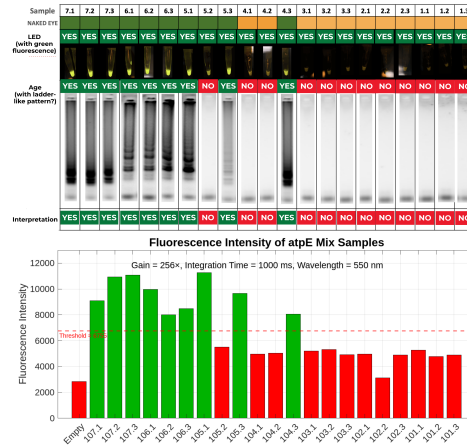


Fig. 11: Bar graph of fluorescence intensity measurements for *atpE* Mix samples together with the results from UPM-NTCBB.

V. FULL SYSTEM ARCHITECTURE

The system operates using a 5 V, 6 A AC/DC power supply, selected based on simulations confirming its capacity to reliably power the microheater and all system components. Real-time data including temperature, fluorescence intensity, and system status are displayed on a 20x4 LCD for user monitoring.

Users control mode selection via physical buttons, enabling independent activation of heating and fluorescence functions to conserve power and extend component lifespan. The software is interrupt-driven, ensuring responsive sensor and user input handling without disrupting system operations. All feedback is managed and displayed locally, eliminating the need for external communication interfaces.

Software-based safety mechanisms include limiting the heater's PWM duty cycle to 70% to prevent overheating.

All components are mounted on a 190 mm × 140 mm PCB enclosed in a compact 3D-printed housing designed in Fusion 360, as illustrated in Figs. 12a, and 12b. The actual physical device printed using Creality Ender 3 is shown in Fig. 12c.

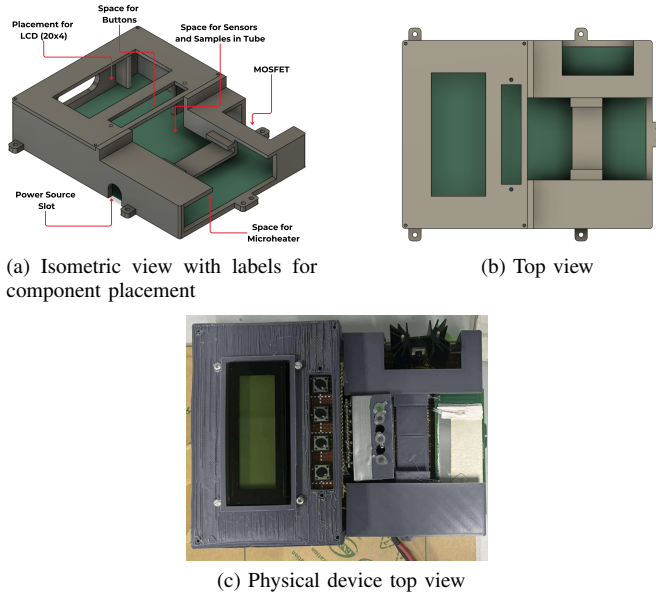


Fig. 12: The 3D model for the testing setup

VI. CONCLUSION

This study demonstrated an integrated microfluidic system for point-of-care testing featuring homogeneous heating via a copper thin-film microheater with PID control, enabling rapid (2–3 min) and stable ($\pm 1^{\circ}\text{C}$) temperatures essential for LAMP, alongside sensitive fluorescence detection using an AS7343 sensor and blue LED excitation to distinguish positive and negative samples. With low power consumption (30 W), a compact footprint, and stand-alone operation, the system shows promise for low-resource settings. However, further calibration of both the heating and fluorescence detection components is needed to optimize performance, particularly by accounting for gene-specific fluorescence threshold levels and by validating the system using actual microfluidic chips instead of PCR tubes. Additionally, future work should incorporate statistical methods, such as receiver operating characteristic (ROC) analysis or confidence interval-based thresholding, to define and validate fluorescence threshold values. This would improve diagnostic reliability and reduce the likelihood of misclassifications in field deployments.

ACKNOWLEDGMENT

The authors would like to extend their sincerest gratitude to PreXDeTEch TB, Center for Integrated Circuits and Device Research (CIDR), and University of the Philippines - Center for Air Research in Urban Environments (UP-CARE) for their invaluable support, including financial assistance and expertise, which significantly contributed to the successful completion of this research.

REFERENCES

- [1] G. Wright and C. Bernstein, *What is point of care (POC) testing? — Definition from TechTarget — techtarget.com*, <https://www.techtarget.com/searchhealthit/definition/point-of-care-POC-testing>, [Accessed 09-12-2024].
- [2] S. Choi, “Powering point-of-care diagnostic devices,” *Biotechnology Advances*, vol. 34, no. 3, 321–330, 2016. DOI: 10.1016/j.biotechadv.2015.11.004.
- [3] S.-M. Yang, S. Lv, W. Zhang, and Y. Cui, “Microfluidic point-of-care (poc) devices in early diagnosis: A review of opportunities and challenges,” *Sensors*, vol. 22, no. 4, 2022, ISSN: 1424-8220. DOI: 10.3390/s22041620. [Online]. Available: <https://www.mdpi.com/1424-8220/22/4/1620>.
- [4] A. K. Yetisen *et al.*, “Paper-based microfluidic system for tear electrolyte analysis,” *Lab on a Chip*, vol. 17, no. 6, 1137–1148, 2017. DOI: 10.1039/c6lc01450j.
- [5] L. C. D. M. S. Taylor J. Moehling Gihoon Choi and R. J. Meagher, “Lamp diagnostics at the point-of-care: Emerging trends and perspectives for the developer community,” *Expert Review of Molecular Diagnostics*, vol. 21, no. 1, pp. 43–61, 2021, PMID: 33474990. DOI: 10.1080/14737159.2021.1873769. eprint: <https://doi.org/10.1080/14737159.2021.1873769>. [Online]. Available: <https://doi.org/10.1080/14737159.2021.1873769>.
- [6] Z. Jeroish, K. Bhuvaneshwari, A. Futane, F. Samsuri, and V. Narayananamurthy, “Design, optimization, fabrication and analysis of cu microheater for loop-mediated isothermal amplification (lamp) applications,” *Materials Today Communications*, vol. 36, p. 106663, 2023, ISSN: 2352-4928. DOI: <https://doi.org/10.1016/j.mtcomm.2023.106663>. [Online]. Available: <https://www.sciencedirect.com/science/article/pii/S2352492823013545>.
- [7] U. Wanderlingh, C. Branca, and S. Vasi, “Portable low-cost autofluorescence analyzer for plankton and plastic detection,” *2021 International Workshop on Metrology for the Sea; Learning to Measure Sea Health Parameters (MetroSea)*, 168–172, 2021. DOI: 10.1109/metrosea52177.2021.9611585.
- [8] Y. Zhang, T.-M. Tseng, and U. Schlichtmann, “Colorisens: An open-source and low-cost portable color sensor board for microfluidic integration with wireless communication and fluorescence detection,” *HardwareX*, vol. 11, 2022. DOI: 10.1016/j.ohx.2022.e00312.
- [9] Z. Jeroish, K. Bhuvaneshwari, A. Futane, F. Samsuri, and V. Narayananamurthy, “Design, optimization, fabrication and analysis of cu microheater for loop-mediated isothermal amplification (lamp) applications,” *Materials Today Communications*, vol. 36, p. 106663, 2023, ISSN: 2352-4928. DOI: <https://doi.org/10.1016/j.mtcomm.2023.106663>. [Online]. Available: <https://www.sciencedirect.com/science/article/pii/S2352492823013545>.